LETTER

doi:10.1038/nature13376

Contribution of semi-arid ecosystems to interannual variability of the global carbon cycle

Benjamin Poulter[1,2], David Frank[3,4], Philippe Ciais[2], Ranga B. Myneni[5], Niels Andela[6], Jian Bi[5], Gregoire Broquet[2], Josep G. Canadell[7], Frederic Chevallier[2], Yi Y. Liu[8], Steven W. Running[9], Stephen Sitch[10] & Guido R. van der Werf[6]

The land and ocean act as a sink for fossil-fuel emissions, thereby slowing the rise of atmospheric carbon dioxide concentrations[1]. Although the uptake of carbon by oceanic and terrestrial processes has kept pace with accelerating carbon dioxide emissions until now, atmospheric carbon dioxide concentrations exhibit a large variability on interannual timescales[2], considered to be driven primarily by terrestrial ecosystem processes dominated by tropical rainforests[3]. We use a terrestrial biogeochemical model, atmospheric carbon dioxide inversion and global carbon budget accounting methods to investigate the evolution of the terrestrial carbon sink over the past 30 years, with a focus on the underlying mechanisms responsible for the exceptionally large land carbon sink reported in 2011 (ref. 2). Here we show that our three terrestrial carbon sink estimates are in good agreement and support the finding of a 2011 record land carbon sink. Surprisingly, we find that the global carbon sink anomaly was driven by growth of semi-arid vegetation in the Southern Hemisphere, with almost 60 per cent of carbon uptake attributed to Australian ecosystems, where prevalent La Niña conditions caused up to six consecutive seasons of increased precipitation. In addition, since 1981, a six per cent expansion of vegetation cover over Australia was associated with a fourfold increase in the sensitivity of continental net carbon uptake to precipitation. Our findings suggest that the higher turnover rates of carbon pools in semi-arid biomes are an increasingly important driver of global carbon cycle inter-annual variability and that tropical rainforests may become less relevant drivers in the future. More research is needed to identify to what extent the carbon stocks accumulated during wet years are vulnerable to rapid decomposition or loss through fire in subsequent years.

Each year, on average, land and ocean carbon sinks absorb the equivalent of about half of the global fossil fuel emissions, thereby providing a critical service that slows the rise in atmospheric CO_2 concentrations[1]. Emissions from fossil fuels and land-use change now exceed ten billion tons or petagrams (Pg) of carbon per year, tracking the most carbon intense emission scenarios of the Intergovernmental Panel on Climate Change[4]. Even with this acceleration, the fraction of anthropogenic emissions that accumulates in the atmosphere (the airborne fraction) has remained largely unchanged since 1959 at 44% (ref. 2) ($P = 0.36$ for slope of linear regression). This implies that the uptake of carbon by ocean and terrestrial processes has, to some extent, kept pace with accelerating emissions owing to a range of possible factors, such as the fertilization effect of increased CO_2 and atmospheric nitrogen deposition on plant growth, changes in growing season length, and land management[5]. In addition to the continued uptake of CO_2, the airborne fraction exhibits large variability on interannual timescales, ranging between 18% and 79% during the past 54 years (ref. 2). This high interannual variability is primarily driven by terrestrial processes, which must be better understood in order for us to be able to forecast long-term biospheric responses to climate change[3].

High uncertainties in quantifying ecosystem processes mean that the global terrestrial carbon sink is often estimated as the residual between emissions from the combustion of fossil fuels, cement production and net land-use change, and sinks combining accumulation in the atmosphere and uptake by the ocean[6]. Using this method, the Global Carbon Project reported in their annual assessment a 2011 residual land sink of 4.1 Pg C yr^{-1} (standard deviation $\pm$ 0.9 Pg C yr^{-1}), representing an unusually large increase compared with the 2.6 $\pm$ 0.8 Pg C yr^{-1} decadal average and the largest reported residual land carbon sink since measurements of atmospheric CO_2 began in 1958. The 2011 residual land sink is indicative of several aspects of the debate surrounding the fate of terrestrial ecosystems under environmental change. First, the large uptake of carbon in 2011 continues a trend of increasing strength in the land carbon sink over at least one decade[1,7]. Second, the large annual growth anomaly in the land carbon sink raises questions regarding the growth rate of atmospheric CO_2 in coming years and how this is affected by the allocation of sequestered carbon to either labile or more stable pools. Lastly, increasing uncertainty in other terms of the global CO_2 budget has direct consequences on land sink estimates, for example, an overestimate of anthropogenic emissions would be assigned (owing to mass conservation and current accounting schemes) as an erroneously large land sink. Thus, attributing changes in net carbon uptake to carbon cycle processes requires a range of methodological approaches.

Here, we investigate the evolution of the terrestrial carbon sink over the past 30 years and the underlying mechanisms of the exceptionally large 2011 residual land carbon sink in a long-term context using (1) a 'bottom-up' process-oriented terrestrial biosphere model, (2) a 'top-down' atmospheric CO_2 inversion and (3) satellite observations of photosynthetic activity and vegetation structure. We allocate net land carbon uptake among specific geographic regions and provide a mechanistic explanation for the climatic and CO_2 response of net primary production (NPP), heterotrophic respiration (R_h), and disturbance that sum up to define net ecosystem exchange (NEE).

We find excellent agreement among the three different terrestrial carbon sink estimates that robustly support record 2011 land carbon uptake (Fig. 1a; with uncertainty presented as $\pm$1 standard deviation). The Lund–Potsdam–Jena (LPJ) dynamic global vegetation model (DGVM; ref. 8) estimates a 2011 land sink of 3.9 $\pm$ 1.3 Pg C yr^{-1}, a 1.3 $\pm$ 0.6 Pg C yr^{-1} anomaly compared to the 2003–2012 mean sink of 2.6 $\pm$ 0.9 Pg C yr^{-1} (Fig. 1a and Extended Data Table 1). Our atmospheric inversion (using the Monitoring Atmospheric Composition and Climate (MACC-II) inversion system; ref. 9) yields a 3.7 $\pm$ 0.4 Pg C yr^{-1} 2011 land sink, equivalent to a 1.0 Pg C yr^{-1} anomaly above the 2.7 $\pm$ 0.4 Pg C yr^{-1} inversion average for 2003–2012. The 2011 land sink estimates by the LPJ DGVM

[1]Montana State University, Institute on Ecosystems and the Department of Ecology, Bozeman, Montana 59717, USA. [2]Laboratoire des Sciences du Climat et de l'Environnement (LSCE), CEA CNRS UVSQ, 91191 Gif Sur Yvette, France. [3]Swiss Federal Research Institute WSL, Dendroclimatology, Zürcherstrasse 111, Birmensdorf 8903, Switzerland. [4]Oeschger Centre for Climate Change Research, University of Bern, CH-3012 Bern, Switzerland. [5]Department of Earth and Environment, Boston University, 685 Commonwealth Avenue, Boston, Massachusetts 02215, USA. [6]Faculty of Earth and Life Sciences, VU University Amsterdam, 1085 De Boelelaan, 1081HV, Amsterdam, The Netherlands. [7]Global Carbon Project, CSIRO, Marine and Atmospheric Research, Canberra, Australian Capital Territory 2601, Australia. [8]ARC Centre of Excellence for Climate Systems Science & Climate Change Research Centre, University of New South Wales, Sydney, New South Wales 2052, Australia. [9]Department of Ecosystem and Conservation Sciences, University of Montana, Missoula, Montana 59812, USA. [10]College of Engineering, Computing and Mathematics, University of Exeter, Exeter EX4 4QF, UK.

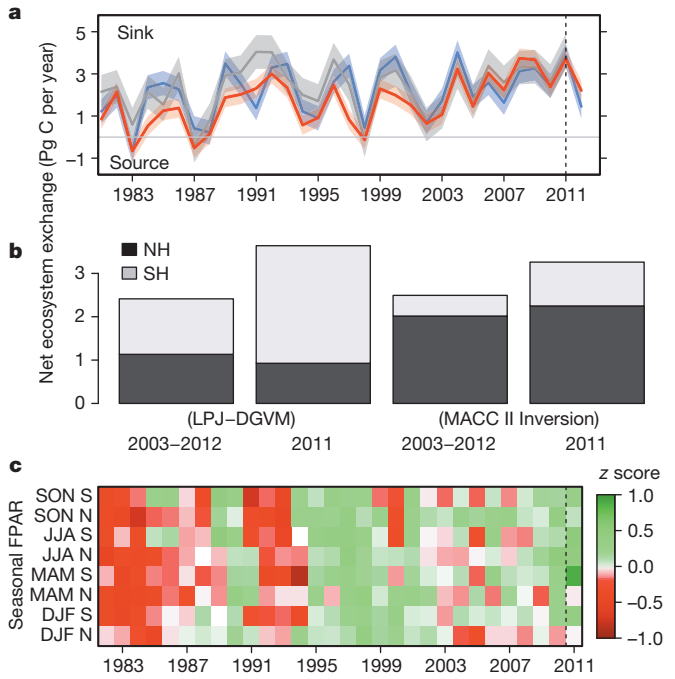

Figure 1 | Interannual variability of NEE and FPAR anomalies. **a**, Annual NEE, where positive values represent carbon uptake, blue is LPJ, red is MACC-II, and the residual land sink is in grey. The standard deviations are ± 0.58 Pg C yr^{-1} for LPJ, ± 0.4 Pg C yr^{-1} for the inversion, and ± 0.8 Pg C yr^{-1} for the residual (see Methods). **b**, Average, 2003–2012, annual NEE for the Northern and Southern hemispheres, estimated by LPJ and the inversion. **c**, AVHRR FPAR anomalies for the southern (S) and northern (N) hemispheres with respect to the 1982–2011 long-term average where the seasonal anomalies were calculated as the z score for each season (s) and each grid cell (i,j) for each year (y); $\mathrm{AVHRR}_{\mathrm{anomaly},ys(i,j)} = \dfrac{\mathrm{AVHRR}_{y,s(i,j)} - \mathrm{AVHRR}_{1982-2011,s(i,j)}}{\sigma\mathrm{AVHRR}_{1982-2011,s(i,j)}}$.

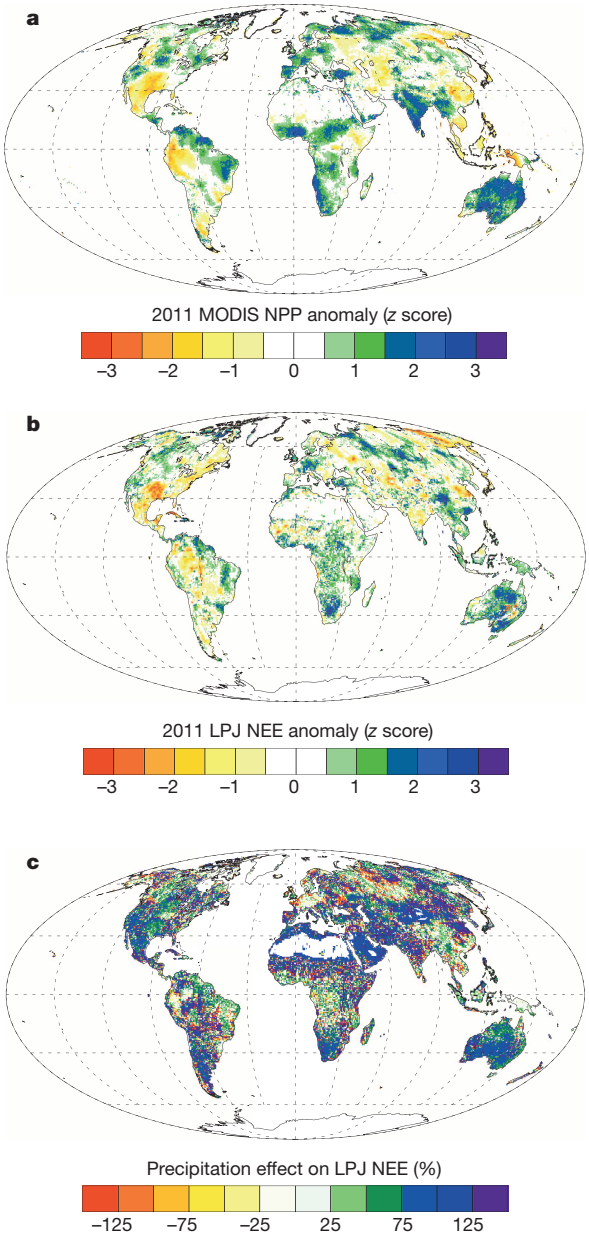

Figure 2 | Global anomalies of NPP and NEE, and the precipitation effect. **a**, Annual NPP anomaly, as z score (defined in Fig. 1), estimated by the MOD17A3 algorithm that uses the MODIS leaf area index (MOD15 Collection 5)[12]. **b**, Annual NEE anomaly, as z score, estimated by the LPJ DGVM, where a positive z score equals a larger sink; the reference period is 2000–2011. **c**, Spatial pattern of the contribution of precipitation to net ecosystem exchange in 2011 calculated as the difference between NEE with the all climate forcing varied and NEE simulated with the precipitation climatology (see Extended Data Fig. 6a and b for the NPP and R_h component fluxes).

and MACC II inversion were greater than the 97.5th percentile over the period 1981–2012, suggesting a convergence of particularly novel ecosystem and climate states.

Both the atmospheric inversion and the DGVM demonstrate an increased contribution from Southern Hemisphere ecosystems to global net carbon uptake in 2011 (Fig. 1b). These patterns are supported by a large observed positive anomaly in the 2010–2011 interhemispheric CO_2 concentration gradient between Mauna Loa (19° N) and the Cape Grim (40° S) monitoring stations[10]. An increase in global NPP appears to be the main driving mechanism behind the 2011 land sink. Global NPP anomalies within the range of 1.7 Pg C simulated from the LPJ model forced with monthly climatic variables from the Climatic Research Unit (CRU) TS3.21 data set (ref. 11) and 1.6 Pg C by the Moderate Resolution Imaging Spectroradiometer (MODIS) NPP algorithm (Fig. 2a), using National Center for Environmental Prediction (NCEP) Reanalysis climate data and a light use-efficiency model[12] provide parallel support for this conclusion. Further investigation shows 79% (MODIS) to 87% (LPJ) of the global NPP anomaly is explained by just three semi-arid regions, Australia, temperate South America and southern Africa, where ecosystem respiration tends to lag productivity, inducing large net carbon uptake (regions AUST, SAmTe and SAf in Fig. 2b and Extended Data Fig. 1)[13–15]. In Australia, for example, compared with the 2003–2012 average, LPJ simulated a 45% increase in NPP for 2011, from an average of 1.75 to 2.54 Pg C yr^{-1}, but only a 9% increase in R_h (from 1.48 to 1.61 Pg C yr^{-1}). Moreover, wetter conditions decreased modelled fire-emissions by 29% (from 0.13 to 0.09 Pg C yr^{-1}) yielding a net 0.84 Pg C 2011 sink. Similarly, we find our conclusions for the greater sensitivity of NPP to precipitation, and lags in R_h, extend to southern Africa and temperate South America. In fact, 51% of the global 2011 net carbon sink was attributed to the three Southern Hemisphere semi-arid regions (Extended Data Table 2), and Australia alone contributed to 57% of the total global LPJ NEE anomaly.

In addition to MODIS, the fraction of photosynthetic active radiation (FPAR) determined from the satellite-borne Advanced Very High Resolution Radiometer (AVHRR), AVHRR-FPAR3g (ref. 16), provides a long-term record of space-borne observations of the fraction of photosynthetic active radiation absorbed. Vegetation greening was widespread globally in 2011, with austral winter (June–August; JJA) FPAR reaching the highest values ever observed in the entire satellite period (1982–2011). In the Southern Hemisphere, record greening (Fig. 1c) was centralized over the same three Southern Hemisphere semi-arid regions (AUST, SAmTe and SAf) and was sustained for nine months spanning

2010 to 2011 (December–February, DJF; March–May, MAM; and JJA). Seasonal FPAR increases over Australia ranged from 4.6% in DJF and 8.7% in MAM to 5.1% in JJA, with all anomalies being prominent extremes in the context of an observed 0.8–1.9% interannual variability over the past 30 years. Notably, 46% (or 34%) of the land area in Australia experienced increases in FPAR in 2011 of more than 2.5 (or 3.0) standard deviations from normal in MAM, with positive FPAR anomalies first developing in eastern Australia in DJF, extending to all of Australia in MAM, then remaining in northern Australia in JJA (Extended Data Fig. 2).

To identify proximate causes for the role of semi-arid regions in the 2011 global sink, we performed a full set of LPJ factorial model simulations to isolate the temperature, precipitation, cloud cover and CO_2 contribution to NEE (Extended Data Table 1; Methods). An additional 'memory' simulation was conducted to evaluate previous-year climate effects that might have contributed to the extraordinary sink in 2011; the 2010 climate was replaced with a near-neutral year (2009) for the El Niño Southern Oscillation (Extended Data Fig. 3). With respect to pre-industrial CO_2 concentrations (287 parts per million, p.p.m.), the LPJ simulations suggest that CO_2 fertilization enhanced the 2011 net carbon uptake by 4.8 Pg C. High precipitation during 2010 and 2011 contributed to 0.62 Pg C and 0.52 Pg C of the global sink, respectively (Fig. 2c), or about 12%, thereby helping to offset land-to-atmosphere CO_2 fluxes driven by long-term negative temperature (−0.84 Pg C) and direct radiative contributions (−0.32 Pg C). In addition, 'memory' effects from 2010 added to the 2011 sink, with the largest difference being a threefold increase in tropical South American NEE when using 2009 climate before 2011. The increase in Amazonian NEE in 2011 was mainly due to recovery from the 2010 Amazon drought[17], which caused a reduction in LPJ NPP and an increase in LPJ R_h in 2010, leading to reduced short-lived litter carbon pools available for respiration and fire in 2011. Although 2011 precipitation explained most of the NEE increase in Australia (a 0.56 Pg C yr^{-1} contribution), the climate memory effect also explained 0.21 Pg C of the 2011 Australian sink because of high precipitation in 2010 that recharged soil moisture and plant carbohydrate reserves to the benefit of NPP in 2011. Among an ensemble of climate indices, the Multivariate El Niño Index (MEI; ref. 18) consistently explained the highest amount of year-to-year variability over Australia for annual carbon uptake (correlation coefficient $r = -0.49$, $P < 0.01$) and DJF FPAR greening ($r = -0.52$, $P < 0.01$) between 1981 and 2011 (Extended Data Fig. 4a–d). This extends earlier findings that found Pacific sea surface temperature as a significant predictor of precipitation-driven greening anomalies as far as South Africa and Australia[19,20]. Notably, the 2010/2011 La Niña—that is, the MEI negative phase—took place over an especially long time period, as observed from multiple satellite, rain gauge and reanalysis data sources (the Tropical Rainfall Measurement Mission (TRMM), CRU and NCEP-DOE; Extended Data Fig. 5a and b), and even lowered global sea levels[21], in addition to altering global carbon uptake[12].

The available evidence points towards an enhanced climatic effect of the 2010/2011 La Niña from interactions with long-term semi-arid region greening trends since the early 1980s at the latest. For example, since 1982, we found an expansion of vegetation across the Australian landscape ($P < 0.01$ for one-sided Kolmogorov–Smirnov test) where land area with FPAR >20% (or 30%) increased by 5.6% (or 3.5%) in the MAM growing season. The greening trend in semi-arid regions has been previously associated with a range of drivers that include altered precipitation frequency and intensity[22], increased water-use efficiency due to elevated CO_2 effects on leaf stomatal conductance[23], and woody encroachment following land-use and grazing[22,24]. Over the same 1982–2011 time period, we observed a statistically significant increase in the sensitivity of LPJ net carbon uptake ($P < 0.001$) and AVHRR-FPAR3g vegetation activity ($P < 0.02$) to austral-autumn precipitation for the Australian continent (Fig. 3a). The observed change in ecosystem sensitivity over Australia meant that an additional 100 mm of growing season (MAM) precipitation led to a fourfold increase in net carbon uptake when comparing sensitivities before (0.2 Pg C yr^{-1} per 100 mm) or after (0.8 Pg C yr^{-1} per 100 mm) 1997, the midpoint of current observational records (1982–2011). An independent data-driven model of net ecosystem production[25], which excluded disturbance processes, confirmed the same statistically robust increase over time in carbon uptake per unit precipitation for Australia (Fig. 3b, $P < 0.001$). Long-term observations from passive-microwave vegetation optical depth (VOD)[26] suggest that the enhanced sensitivity of vegetation to climate is a result of both increases in grass cover as well as from woody encroachment (Fig. 3c).

The 2011 land carbon sink anomaly indicates a novel climate-driven response of the biosphere where interactions between extremes in austral precipitation[27] and changes in land cover[23] (both possibly caused by humans) are contributing to non-analogue ecosystem behaviour with global biogeochemical significance. We propose that the current paradigm, whereby tropical rainforest El Nino/Southern Oscillation coupling dominates interannual variability of the atmospheric CO_2 growth rate[3,28], may become less relevant in the future. We explored whether semi-arid carbon-cycle climate sensitivity feedbacks exist among an ensemble of 15 Earth system models contributed to the Coupled Model Intercomparison Project Phase 5 (CMIP5; ref. 29). In contrast to our observations, we found that for semi-arid regions, modelled carbon uptake and precipitation sensitivity remains relatively stable over the 1990 to 2090 period for the CMIP5 ensemble ($P = 0.33$, one-sided Student's t-test, Fig. 4). This suggests that processes contributing to the novel ecosystem dynamics identified here may be overlooked in future climate change scenarios. As the dynamics of dryland systems, which cover 45% of the Earth's land surface, increase in global importance, more

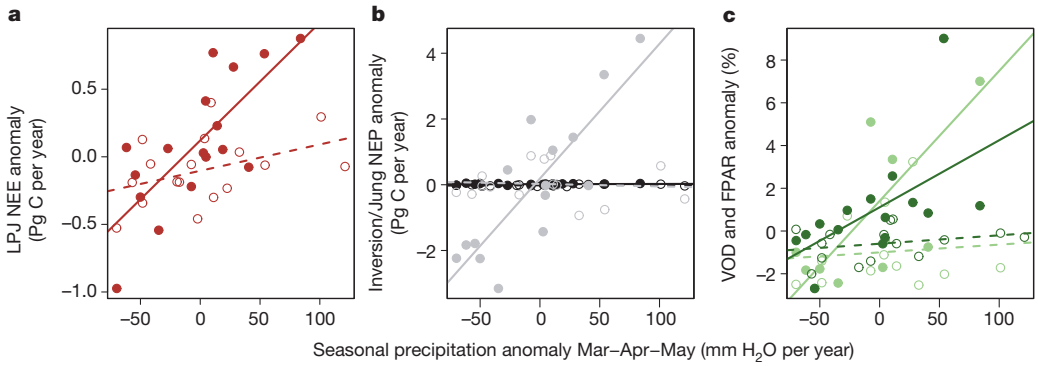

Figure 3 | Change in climate sensitivity of observations for Australia. **a**, Climate sensitivity of annual LPJ NEE anomalies to MAM precipitation anomalies for Australia. The open circles and dashed line are the points and regression line for 1982–1996 (β_1) and the closed circles and solid line are for 1997–2011 ($\beta_1 + \beta_3$), from the following linear regression model using NEE and precipitation anomalies ($P_{anomaly}$) where A is an indicator variable for the different time periods: ($NEE_{anomaly} = \beta_0 + \beta_1 P_{anomaly} + \beta_2 A + \beta_3 P_{anomaly} A$). **b**, Climate sensitivity of annual NEE from the MACC-II inversion (black symbols) and the upscaled NEP product (grey symbols) using the same linear model as in **a**. **c**, Climate sensitivity of annual VOD (light green symbols) and MAM FPAR (dark green symbols) also using the model described in **a**.

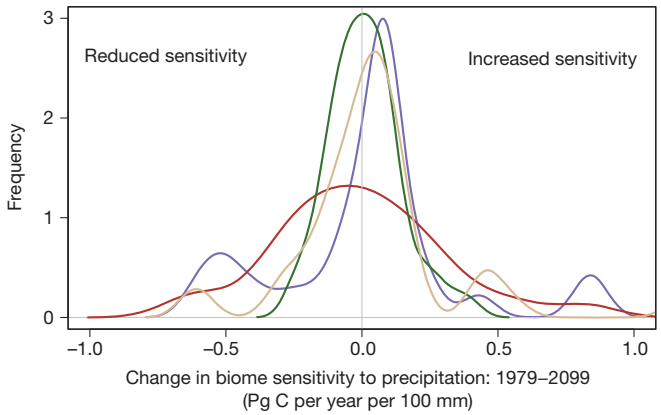

Figure 4 | Change in regional climate sensitivity of CMIP5 models. Distribution of the change in sensitivity between the periods 1979–2005 and 2069–2095 in net biome production to annual precipitation for four biomes ($n = 15$ CMIP5 Earth System Models). Precipitation sensitivity was estimated as β_1 while controlling for changes in sensitivity due to CO_2 and air temperature $NBP_{anomaly} = \beta_0 + \beta_1 CO_2^{anomaly} + \beta_2 P^{anomaly} + \beta_3 T^{air}_{anomaly}$. The different lines refer to tropical (green), temperate (brown), semi-arid (tan), and boreal (purple) biomes.

research is needed to identify whether enhanced carbon sequestration in wet years is particularly vulnerable to rapid decomposition or loss through fire in subsequent years, and is thus largely transitory. Such behaviour may already be reflected by the larger-than-average atmospheric growth rate in 2012 (ref. 30) that was associated with a return to near-normal terrestrial land sink conditions (Fig. 1a).

METHODS SUMMARY

We use multiple data sources, including carbon accounting methods, carbon-cycle model simulations, and satellite-based vegetation products to investigate the magnitude and mechanisms driving variability in the terrestrial carbon sink. NPP (the total photosynthesis minus plant autotrophic respiration losses) is simulated by the LPJ DGVM and also estimated independently with the MODIS NPP algorithm, MOD17A3. The balance between carbon uptake from NPP and losses from soil respiration and disturbance (NEE) is quantified from the Global Carbon Project, the LPJ DGVM, and the MACC-II atmospheric inversion system (http://www.copernicus-atmosphere.eu/). NEP (the balance between gross carbon inputs from photosynthesis and losses from ecosystem respiration, excluding disturbance) is estimated from upscaled gridded flux tower observations. Optical and passive microwave satellite data are employed to assess vegetation greenness trends (AVHRR FPAR3g) and vegetation structure or vegetation optical depth (VOD). Monthly and seasonal precipitation fluctuation is quantified from TRMM 3B43v7 (http://mirador.gsfc.nasa.gov) and NCEP-DOE Reanalysis II (http://www.esrl.noaa.gov), and the Climatic Research Unit (CRU) TS3.21 (http://www.cru.uea.ac.uk/). Regional summaries of the global gridded data followed boundaries from the eleven land regions specified in the TRANSCOM atmospheric inversion experiment. We further differentiate North and South Africa to distinguish between wet and semi-arid climates with the ratio of precipitation to potential evaporation set to 0.7. Historical (1860–2005) simulations of net biome production, equivalent to NEE, from the Fifth Coupled Model Intercomparison Project (CMIP5) are merged with the Representative Concentration Pathway 8.5 (RCP8.5) to create temporal composites spanning 1860–2099 for 15 Earth system models.

Online Content Any additional Methods, Extended Data display items and Source Data are available in the online version of the paper; references unique to these sections appear only in the online paper.

Received 2 August 2013; accepted 10 April 2014.
Published online 21 May 2014.

1. Ballantyne, A. P., Alden, C. B., Miller, J. B., Tans, P. P. & White, J. W. C. Increase in observed net carbon dioxide uptake by land and oceans during the past 50 years. *Nature* **488,** 70–72 (2012).
2. Le Quéré, C. *et al.* The global carbon budget 1959–2011. *Earth Syst. Sci. Data* **5,** 1107–1157 (2013).
3. Cox, P. *et al.* Sensitivity of tropical carbon to climate change constrained by carbon dioxide variability. *Nature* **494,** 341–344 (2013).
4. Peters, G. P. *et al.* The challenge to keep global warming below 2 °C. *Nature Clim. Change* **3,** 4–6 (2012).
5. Pan, Y. *et al.* A large and persistent carbon sink in the world's forests. *Science* **333,** 988–993 (2011).
6. Canadell, J. G. *et al.* Contributions to accelerating atmospheric CO_2 growth from economic activity, carbon intensity, and efficiency of natural sinks. *Proc. Natl Acad. Sci. USA* **104,** 18866–18870 (2007).
7. Sitch, S. *et al.* Trends and drivers of regional sources and sinks of carbon dioxide over the past two decades. *Biogeosci. Disc.* **10,** 20113–20177 (2013).
8. Sitch, S. *et al.* Evaluation of ecosystem dynamics, plant geography and terrestrial carbon cycling in the LPJ dynamic global vegetation model. *Glob. Change Biol.* **9,** 161–185 (2003).
9. Chevallier, F. *et al.* CO_2 surface fluxes at grid point scale estimated from a global 21 year reanalysis of atmospheric measurements. *J. Geophys. Res. D* **115,** D21307 (2010).
10. Francey, R. J. *et al.* Atmospheric verification of anthropogenic CO_2 emission trends. *Nature Clim. Change* **3,** 520–524 (2013).
11. Harris, I., Jones, P. D., Osborn, T. J. & Lister, D. H. Updated high-resolution grids of monthly climatic observations – the CRU TS3.10 Dataset. *Int. J. Climatol.* **34,** 623–642 (2013).
12. Bastos, A., Running, S. W., Gouveia, C. & Trigo, R. M. The global NPP dependence on ENSO: La-Niña and the extraordinary year of 2011. *J. Geophys. Res.* **118,** 1247–1255 (2013).
13. Haverd, V. *et al.* Multiple observation types reduce uncertainty in Australia's terrestrial carbon and water cycles. *Biogeosciences* **10,** 2011–2040 (2013).
14. Haverd, V. *et al.* The Australian terrestrial carbon budget. *Biogeosciences* **10,** 851–869 (2013).
15. Rotenberg, E. & Yakir, D. Contribution of semi-arid forests to the climate system. *Science* **327,** 451–454 (2010).
16. Zhu, Z. *et al.* Global Data Sets of Vegetation LAI3g and FPAR3g derived from GIMMS NDVI3g for the period 1981 to 2011. *Remote Sens.* **5,** 927–948 (2013).
17. Marengo, J. A., Tomasella, J., Alves, L. M., Soares, W. R. & Rodriguez, D. A. The drought of 2010 in the context of historical droughts in the Amazon region. *Geophys. Res. Lett.* **38,** L12703 (2011).
18. Wolter, K. & Timlin, M. S. Monitoring ENSO in COADS with a seasonally adjusted principal component index. In *Proc. 17th Climate Diagnostics Workshop* 52–57 (NOAA/NMC/CAC, NSSL, Univ. Oklahoma, 1993).
19. Myneni, R. B., Los, S. O. & Tucker, C. J. Satellite-based identification of linked vegetation index and sea surface temperate anomaly areas from 1982–1990 for Africa, Australia and South America. *Geophys. Res. Lett.* **23,** 729–732 (1996).
20. Woodward, F. I., Lomas, M. R. & Quaife, T. Global responses of terrestrial productivity to contemporary climatic oscillations. *Phil. Trans. R. Soc. Lond. B* **363,** 2779–2785 (2008).
21. Boening, C., Willis, J. K. Landerer, F. W., Nerem, R. S. & Fasullo, J. The 2011 La Niña: so strong, the oceans fell. *Geophys. Res. Lett.* **39,** doi:10.1029/2012GL053055 (2012).
22. Donohue, R. J., McVicar, T. R. & Roderick, M. L. Climate-related trends in Australian vegetation cover as inferred from satellite observations, 1981–2006. *Glob. Change Biol.* **15,** 1025–1039 (2009).
23. Donohue, R. J., Roderick, M. L., McVicar, T. R. & Farquhar, G. D. CO_2 fertilisation has increased maximum foliage cover across the globe's warm, arid environments. *Geophys. Res. Lett.* **40,** 3031–3035 (2013).
24. Asner, G. P., Elmore, A. J., Olander, L. P., Martin, R. E. & Harris, A. T. Grazing systems, ecosystem responses, and global change. *Annu. Rev. Environ. Resour.* **29,** 261–299 (2004).
25. Jung, M., Reichstein, M. & Bondeau, A. Towards global empirical upscaling of FLUXNET eddy covariance observations: validation of a model tree ensemble approach using a biosphere model. *Biogeosciences* **6,** 5271–5304 (2009).
26. Andela, N., Liu, Y. Y., van Dijk, A. I. J. M., de Jeu, R. A. M. & McVicar, T. R. Global changes in dryland vegetation dynamics (1988–2008) assessed by satellite remote sensing: combining a new passive microwave vegetation density record with reflective greenness data. *Biogeosci.* **10,** 6657–6676 (2013).
27. Kang, S. M. *et al.* Modeling evidence that ozone depletion has impacted extreme precipitation in the austral summer. *Geophys. Res. Lett.* **40,** 4054–4059 (2013).
28. Wang, W. *et al.* Variations in atmospheric CO_2 growth rates controlled by tropical temperature. *Proc. Natl Acad. Sci. USA* doi:10.1073/pnas.1219683110 (2013).
29. Taylor, K. E., Stouffer, R. J. & Meehl, G. A. An overview of the CMIP5 and the experimental design. *Bull. Am. Meteorol. Soc.* **93,** 485–498 (2012).
30. Le Quéré, C. *et al.* Global carbon budget 2013. *Earth Syst. Sci. Data Discuss.* **6,** 689–760 (2013).

Acknowledgements We acknowledge support from the EU FP7 GEOCARBON programme (283080), and thank the researchers involved with collecting and maintaining the climate data at the Climate Research Unit, University of East Anglia, UK, and the National Center for Atmospheric Research, USA. We also acknowledge the World Climate Research Programme's Working Group on Coupled Modelling, which is responsible for CMIP. We thank the climate modelling groups for producing and making available their model output. For CMIP the US Department of Energy's Program for Climate Model Diagnosis and Intercomparison provides coordinating support and led development of software infrastructure in partnership with the Global Organization for Earth System Science Portals. We also thank M. Jung for providing the 'upscaled' NEE data used in our analysis. J.G.C. acknowledges the support of the Australian Climate Change Science Program. R.B.M. and S.W.R. were funded by the NASA Earth Science Division. C. Le Quéré and L. Cernusak provided comments and suggestions that improved the manuscript. This paper is a contribution to the Global Carbon Budget activity of the Global Carbon Project.

Author Contributions B.P., D.F., P.C. and R.B.M. designed the analyses. J.B., F.C., G.B., D.F., R.B.M., S.W.R., S.S., G.R.v.d.W., J.G.C., Y.Y.L. and N.A. contributed data to the analyses. B.P., F.C., R.B.M., S.R. and D.F. conducted the analyses. All authors contributed to the writing of the manuscript.

Author Information Reprints and permissions information is available at www.nature.com/reprints. The authors declare no competing financial interests. Readers are welcome to comment on the online version of the paper. Correspondence and requests for materials should be addressed to B.P. (benjamin.poulter@montana.edu).

METHODS

Carbon fluxes and their uncertainties. We follow the carbon-cycle definitions summarized by ref. 31 when describing the net land carbon sink in terms of NEE or NEP and associated component fluxes. Data for estimating the airborne fraction, the residual land sink and its anomalies were obtained online from the Global Carbon Project[2] (version 1.5) for the years 1959–2011. Uncertainties are presented as ± 1 standard deviation (σ), assuming Gaussian error and a 68% likelihood that the true value is within this range. The LPJ DGVM was run with the GlobFirm fire module enabled and fully prognostic dynamic natural vegetation (excluding land-cover change). The CRU TS3.21 climate data set[11] was used for LPJ model simulations starting in 1901 and ending in 2012 with observed rising CO_2 concentrations from ice-core measurement of CO_2 and then the Mauna Loa Observatory after 1958. Uncertainty in LPJ NEE was estimated using a Latin hypercube approach to generate 200 parameter sets and corresponding simulations at 1-degree spatial resolution for 13 of the most important parameters[32]. The observed linear relationship between the Latin hypercube model ensemble global mean NEE and its standard deviation ($R^2 = 0.62$) was used to predict the 2011 land sink uncertainty for the 0.5-degree simulation. Uncertainty from climate forcing was considered by comparing different climate data sets (see below) and is not likely to affect annual anomalies or trends in carbon fluxes[33]. LPJ simulates semi-arid plant functional types by a mix of grasses with C_3 and C_4 photosynthetic pathways and, in lesser abundance, tropical and temperate trees. Carbon cycle fluxes simulated by LPJ were in close agreement with regionally parameterized models for Australia, such as CABLE[14], and regional NPP from satellite-based estimates of MODIS (Extended Data Table 2). Simulated losses of carbon from fire and their anomalies were benchmarked with the GFAS v1.0 (ref. 34) and GFED v3.1 (ref. 35) data sets that use satellite-observed fire radiative power and burned area, respectively, to estimate carbon emissions (Extended Data Table 3). The atmospheric inversion was based on the MACC-II inversion system version 12.1, described in ref. 9, using atmospheric CO_2 data sets from a global network (NOAA/ESRL, WDCGG, CarboEurope and RAMCES) of continuous and discrete flask samples, with a climatological prior for NEP land-surface carbon fluxes from the ORCHIDEE DGVM[9] and fire emissions from GFED v2.1 (ref. 36) until 2011, and the long-term mean substituted for 2012. The inversion is applied on a 3.75×2.5 degree grid with fluxes inverted at weekly resolution and night-time and daytime fluxes separated. The MACC-II inversion minimizes a Bayesian objective function, assuming errors are Gaussian (posterior errors presented here as ± 1 standard deviation), and error correlation implied by off-diagonal elements in the posterior error covariance matrix. Upscaled flux tower observations were the basis for the data-derived NEE model of ref. 25, representing monthly 0.5-degree fluxes from 1982 to 2011. The MODIS (MOD17A3[37]) product provided annual NPP data at 1-km resolution and was resampled to a resolution of 8 km to match AVHRR-FPAR3g before analysis. Net biome production from the CMIP5 RCP8.5 ensemble[29,38] was merged with the corresponding historical simulations to create temporal composites covering the years 1860–2099 for 15 Earth system models (Extended Data Table 4).

Vegetation activity. Measurements of FPAR were modelled from surface reflectance observed aboard the AVHRR and incorporated into the FPAR3g[16] data set (1981–2011). The FPAR3g bimonthly data set was first filtered for low values, within the range of uncertainty (<2.5%), before compositing to monthly values using a maximum values approach. Gridded passive microwave measurements of VOD from[39] were aggregated from 0.25-degree resolution to each of the thirteen regional means at a monthly resolution from 1988 to 2011. The VOD is an indicator of water content in both woody and leaf components of aboveground biomass. The VOD time series is based on a multi-source data set consisting of harmonized passive microwave measurements from SSM/I (Special Sensor Microwave Imager, 1988–2007) and AMSR-E (the Advanced Microwave Scanning Radiometer – Earth Observing System, July 2002–September 2011) sensors[39].

Climate data sets. Precipitation data from satellite (TRMM 3B43v7), reanalysis (NCEP-DOE Reanalysis II[40], 1979-2012), and ground-based observations (CRU TS3.21[11]) were compared with one another for annual and seasonal similarities (Extended Data Fig. 5a and b). Over Australia, annual precipitation was observed as up to $+205 \pm 54$ mm (in 2010) and $+178 \pm 71$ mm (in 2011) above the long-term annual average of 555 ± 23 mm yr^{-1}, with uncertainties presented as the standard deviation of the three products. An ensemble of climate indices were evaluated (Extended Data Fig. 4a–d) with data for the MEI from ref. 18, where negative values indicate the La Niña climate mode.

31. Chapin, F. S. *et al.* Reconciling carbon-cycle concepts, terminology, and methods. *Ecosystems* **9,** 1041–1050 (2006).
32. Zaehle, S., Sitch, S., Smith, B. & Hattermann, F. Effects of parameter uncertainty on the modeling of terrestrial biosphere dynamics. *Glob. Biogeochem. Cycles* **19,** GB3020, doi:3010.1029/2004GB002395 (2005).
33. Poulter, B., Frank, D., Hodson, E. L., Lischke, H. & Zimmermann, N. E. Impacts of land cover and climate data selection on understanding terrestrial carbon dynamics and the CO_2 airborne fraction. *Biogeosciences* **8,** 2027–2036 (2011).
34. Kaiser, J. W. *et al.* Biomass burning emissions estimated with a global fire assimilation system based on observed fire radiative power. *Biogeosciences* **9,** 527–554 (2012).
35. van der Werf, G. R. *et al.* Global fire emissions and the contribution of deforestation, savanna, forest, agricultural, and peat fires (1997–2009). *Atmos. Chem. Phys. Discuss.* **10,** 16153–16230 (2010).
36. van der Werf, G. R. *et al.* Interannual variability in global biomass burning emissions from 1997-2004. *Atmos. Chem. Phys.* **6,** 3423–3441 (2006).
37. Zhao, M. & Running, S. W. Drought-induced reduction in global terrestrial net primary production from 2000 through 2009. *Science* **329,** 940–943 (2010).
38. Moss, R. H. *et al.* The next generation of scenarios for climate change research and assessment. *Nature* **463,** 747–756 (2010).
39. Liu, Y. Y., van Dijk, A. I. J. M., McCabe, M. F., Evans, J. P. & de Jeu, R. A. M. Global vegetation biomass change (1988–2008) and attribution to environmental and human drivers. *Glob. Ecol. Biogeogr.* **6,** 692–705 (2012).
40. Kanamitsu, M. *et al.* NCEP-DEO AMIP-II Reanalysis (R-2). *Bull. Am. Meteorol. Soc.* **83,** 1631–1643 (2002).

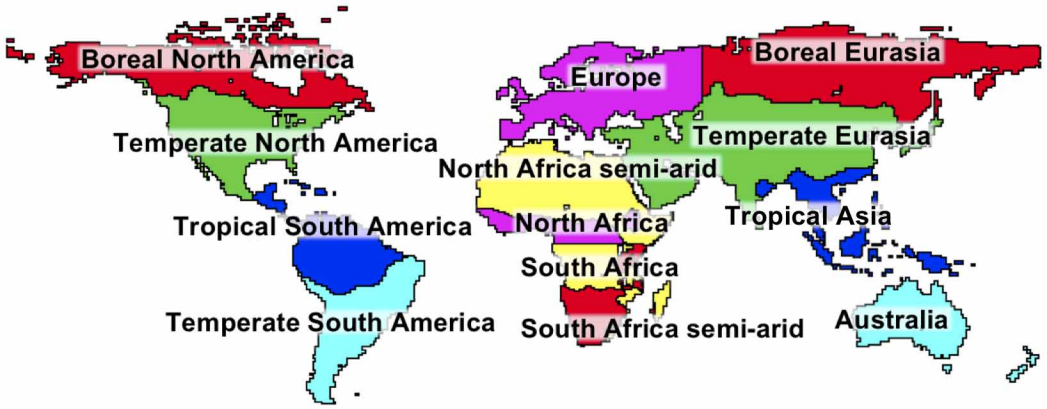

Extended Data Figure 1 | The thirteen regions used throughout the analysis, 11 from TRANSCOM, and two additional regions for the African continent that are semi-arid (see Methods Summary).

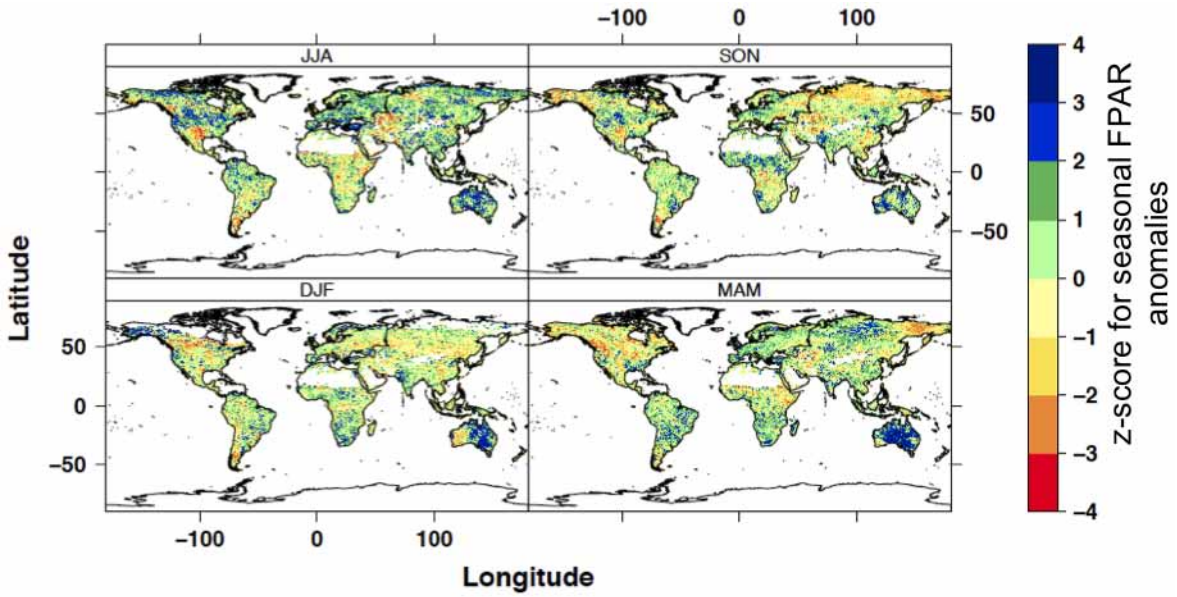

Extended Data Figure 2 | Seasonal AVHRR FPAR anomalies (*z* score) for the year 2011. The *z* score is calculated relative to the long-term seasonal mean and standard deviation of FPAR (1982–2011); see legend to Fig. 1c. The seasons DJF, MAM, JJA and SON are defined by the first letter of each month.

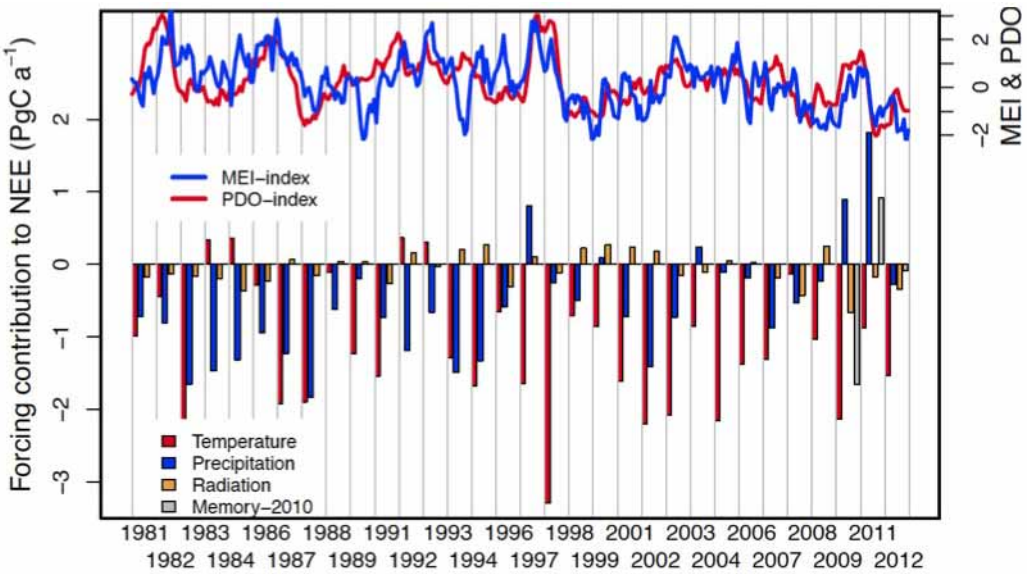

Extended Data Figure 3 | Forcing contribution to NEE and the MEI and PDO indices. The full climate attribution of the global land sink simulation by the LPJ DGVM is shown in the bar graph. PDO, Pacific Decadal Oscillation.

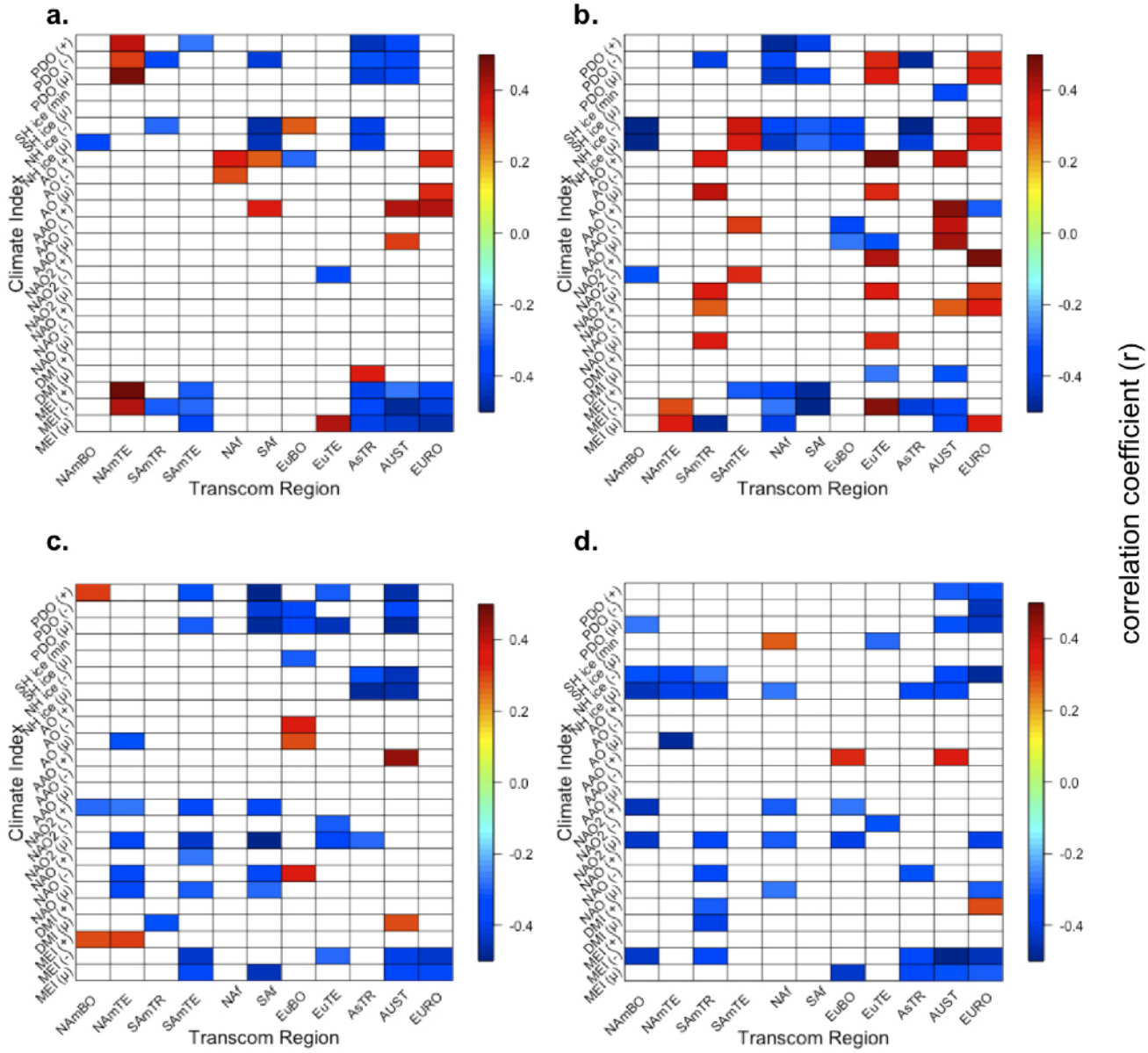

Acronym	Climate mode, or proxy, and data source
PDO	Pacific Decadal Oscillation (NOAA)
SH ice	Southern Hemisphere ice extent (NSIDC)
NH ice	Northern Hemisphere ice extent (NSIDC)
AO	Arctic Oscillation (NOAA)
AAO	Antarctic Oscillation (NOAA)
NAO2	North Atlantic Oscillation (NOAA)
NAO	Hurrel North Atlantic Oscillation (NCAR)
DMI	Dipole Mode Index (JAMSTEC)
MEI	Multivariate ENSO Index (NOAA)

*Transcom regions are defined in Extended Data Fig. 1
*Correlations of seasonal NEE and FPAR were made with the climate mode's annual mean (μ), minimum (-), and maximum (+) value
*NOAA - National Oceanic and Atmospheric Administration; NSIDC – National Snow and Ice Data Center; NCAR – National Center for Atmospheric Research; JAMSTEC – Japan Agency for Marine Earth Science and Technology

Extended Data Figure 4 | *r* and FPAR correlations between climate modes for NEE at given seasons. Shown is *r* (on the colour scales) between climate modes and MAM (**a**), and JJA (**b**) NEE simulated by LPJ for each of the TransCom regions. FPAR correlations between climate modes are shown for MAM (**c**) and JJA (**d**). The correlations were made for 1982–2011. Blank boxes indicate correlation between −0.1 and 0.1.

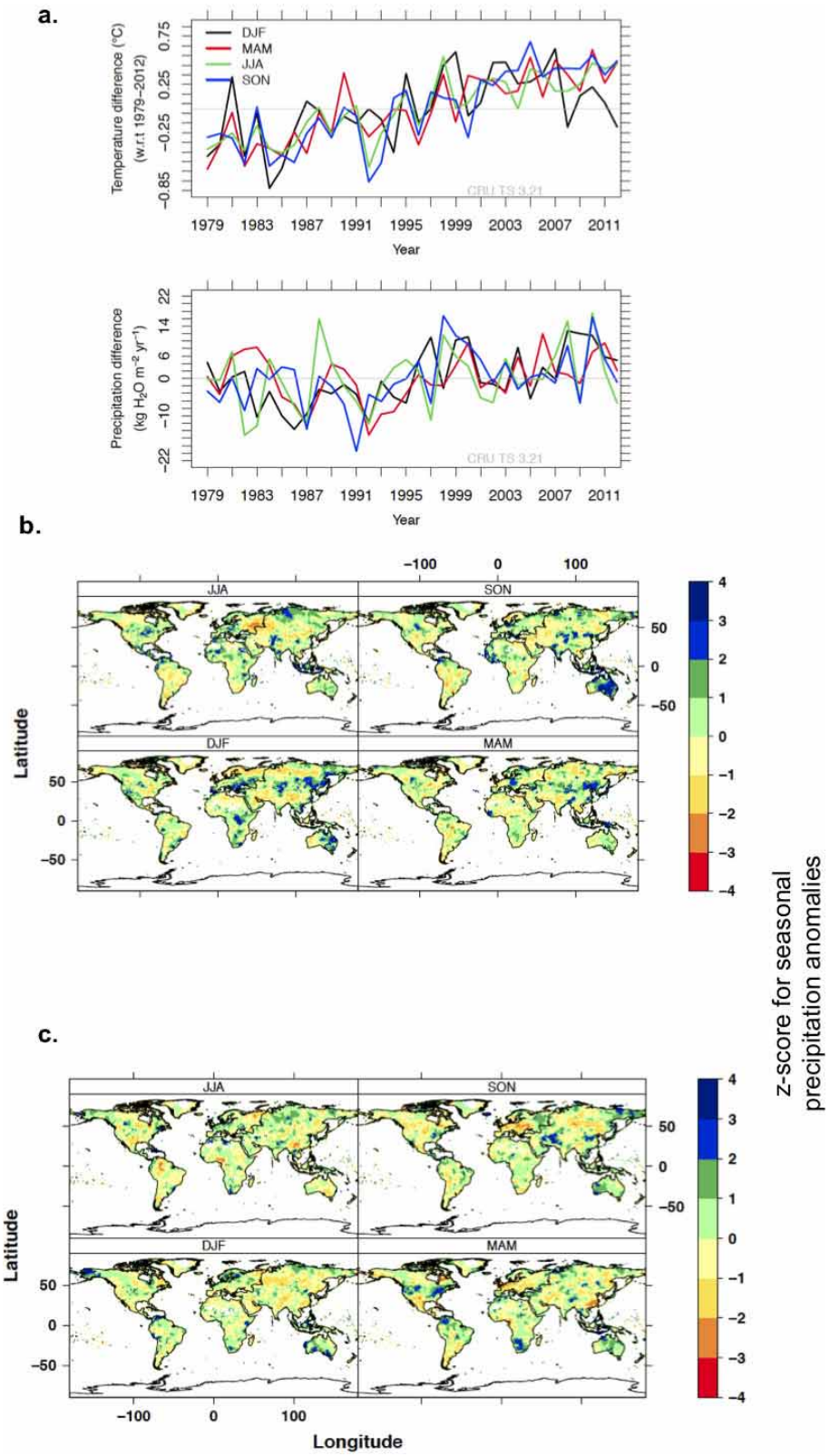

Extended Data Figure 5 | Global climate anomalies for air temperature and precipitation. **a**, Global temperature and precipitation anomalies from CRU TS3.21 data. The anomalies are with respect to 1979–2012 seasonal means. **b**, Seasonal precipitation anomalies (*z* score) for year 2010. **c**, Seasonal precipitation anomalies (*z* score) for year 2011. The *z* score for **b** and **c** is calculated relative to the long-term seasonal mean and standard deviation of precipitation (1979–2011).

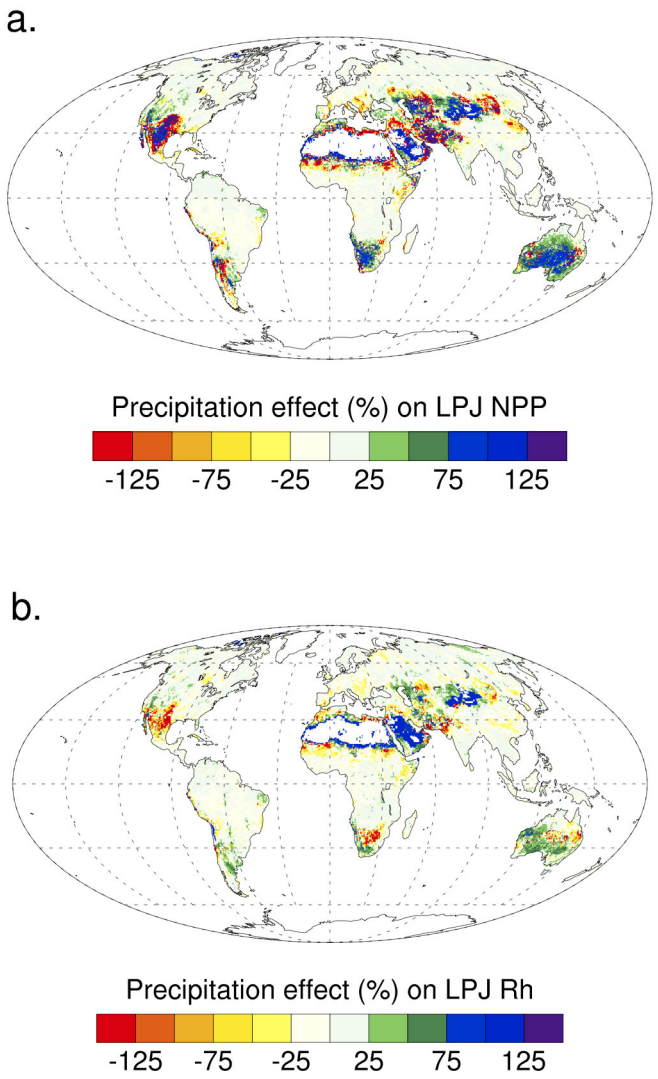

Extended Data Figure 6 | Spatial pattern of the contribution of precipitation to NEE exchange in 2011. This is calculated as the difference between NPP (**a**) and R_h (**b**) with the all-climate forcing varied and NEE simulated with the precipitation climatology. This is the same as in Fig. 2c but for component fluxes of NEE.

Extended Data Table 1 | Global summary of annual NEE

Carbon flux	Data Source	All climate and CO_2 drivers varying			Constant Temp.	Constant Precip.	Constant Clouds	Pre-industrial CO_2	Memory Effect
		2003-2012	2011	2012	2011	2011	2011	2011	2011
Net ecosystem exchange	Residual	2.91	4.57	2.38	-	-	-	-	-
	LPJ	2.59	3.86	1.45	4.70	3.39	4.18	-0.94	3.10
	MACC-II Inversion	2.67	3.71	2.21	-	-	-	-	-
Net Primary Production (NPP)	MODIS-NPP (MOD17A3)	53.0	54.5	52.9	-	-	-	-	-
	LPJ	61.15	62.74	60.54	62.73	62.83	63.11	52.76	62.17
Heterotrophic respiration (Rh)	LPJ	54.65	54.90	54.85	53.89	55.33	54.69	50.77	54.45
Fire emissions (FIRE)	LPJ	3.90	3.98	4.24	4.12	4.11	4.00	3.08	3.92
	GFED v3.1	1.93	1.63	-	-	-	-	-	-
	GFAS v1.0	1.87	1.82	1.89	-	-	-	-	-

NEE = NPP − R_h − fire. Its component fluxes are estimated from LPJ, the residual, the MACC-II inversion, and from MODIS, GFED and GFAS. All units are in Pg C yr^{-1}.

Extended Data Table 2 | Annual LPJ-derived NEE

TransCom Region	2011 Anomalies					2012 Anomalies				
	NEE	NPP	MODIS NPP	Rh	Fire	NEE	NPP	MODIS NPP	Rh	Fire
Boreal North America	-0.04	0.01	0.04	0.03	0.01	-0.05	0.04	0.13	0.05	0.04
Temperate North America	-0.45	-0.45	-0.24	-0.06	0.05	-0.71	-0.60	-0.23	0.06	0.05
Tropical South America	-0.02	0.12	0.02	0.14	-0.02	0.12	0.10	0.0	-0.05	0.02
Temperate South America	0.28	0.27	0.26	0.02	-0.04	-0.20	-0.13	-0.26	-0.09	0.15
North Africa	0.13	0.07	0.37	-0.09	0.04	0.21	0.17	0.46	-0.02	-0.01
South Africa	0.32	0.26	0.45	-0.07	0.01	-0.01	-0.07	0.14	-0.09	0.03
Boreal Europe	0.08	0.26	0.06	0.19	0.01	-0.14	-0.12	-0.06	-0.06	0.08
Temperate Europe	0.06	-0.0	0.12	-0.09	0.03	-0.04	0.02	0.04	0.05	0.01
Tropical Asia	0.13	0.13	-0.16	0.01	-0.01	0.0	0.07	-0.14	0.08	-0.02
Australia	0.70	0.79	0.57	0.13	-0.04	-0.01	0.06	0.07	0.06	0.01
Europe	0.02	0.07	0.14	0.0	0.05	-0.31	-0.16	-0.18	0.17	-0.03

Also shown are the component flux anomalies (Pg C yr^{-1}) for each of the 11 TransCom regions (see **Extended Data Fig. 1** for region map). The annual LPJ anomalies for 2011 and 2012 are calculated relative to the 2003 to 2012 time period. MODIS NPP anomalies, with respect to 2000–2011, are provided in grey text for comparison (but not used in the NEE calculation). A positive NEE anomaly indicates an increase in the carbon sink strength and negative fire anomalies mean a decrease in fire emissions. The total global LPJ NEE anomaly for 2011 was 1.4 Pg C yr^{-1}.

Extended Data Table 3 | Total carbon emissions from wildfire for each TransCom region

TransCom Region	LPJ			GFAS			GFED		
	2002-2011	2011	2012	2002-2011	2011	2012	2002-2011	2011	2012
Boreal North America	0.16	0.17	0.21	0.05	0.05	0.04	0.06	0.05	
Temperate North America	0.27	0.33	0.33	0.05	0.07	0.06	0.02	0.03	
Tropical South America	0.48	0.47	0.51	0.2	0.1	0.12	0.22	0.11	
Temperate South America	0.44	0.42	0.61	0.14	0.11	0.13	0.11	0.06	No data
North Africa	0.47	0.5	0.45	0.37	0.38	0.27	0.46	0.39	
South Africa	0.57	0.58	0.6	0.48	0.52	0.47	0.56	0.56	
Boreal Europe	0.25	0.26	0.34	0.16	0.12	0.28	0.13	0.09	
Temperate Europe	0.44	0.47	0.45	0.04	0.03	0.04	0.03	0.02	
Tropical Asia	0.23	0.22	0.21	0.16	0.12	0.15	0.24	0.12	
Australia	0.15	0.09	0.14	0.13	0.25	0.25	0.12	0.16	
Europe	0.26	0.3	0.23	0.02	0.01	0.02	0.02	0.01	

Emissions are estimated from LPJ, and the GFAS[34] and GFED[35] data sets for the matching 2002–2012 averaging period, and for the years 2011 and 2012. Units are Pg C yr^{-1}.

Extended Data Table 4 | CMIP5 Earth system models from PCMDI node 9 that were accessed and where the RCP8.5 scenario (2005–2099) was merged with the historical simulation (1860–2005)

Model Name (PCMDI node 9)	Net Biome Production		Air temperature		Precipitation	
	Historical	RCP 8.5	Historical	RCP 8.5	Historical	RCP 8.5
ACCESS1-0			✔	✔	✔	✔
ACCESS1-3			✔	✔	✔	✔
CanCM4			✔		✔	
CanESM2	✔	✔	✔	✔	✔	✔
CCSM4	✔	✔	✔	✔	✔	✔
CESM1-BGC	✔			✔		✔
CESM1-CAM5	✔			✔		✔
CESM1-FASTCHEM	✔					
CESM1-WACCM	✔			✔		✔
CMCC-CESM		✔	✔	✔	✔	✔
CMCC-CM			✔	✔	✔	✔
CMCC-CMS			✔	✔	✔	✔
CNRM-CM5-2			✔		✔	
CNRM-CM5			✔	✔	✔	✔
CSIRO-Mk3-6-0			✔	✔	✔	✔
EC-EARTH			✔	✔	✔	✔
FGOALS-g2			✔	✔	✔	✔
FIO-ESM			✔	✔	✔	✔
GFDL-CM3			✔	✔	✔	✔
GFDL-ESM2G		✔	✔	✔	✔	✔
GFDL-ESM2M	✔	✔	✔	✔	✔	✔
GISS-E2-H-CC			✔		✔	
GISS-E2-H			✔	✔	✔	✔
GISS-E2-R-CC			✔		✔	
GISS-E2-R			✔	✔	✔	✔
HadCM3			✔		✔	
HadGEM2-AO			✔	✔	✔	✔
HadGEM2-CC	✔	✔	✔	✔	✔	✔
HadGEM2-ES	✔	✔	✔	✔	✔	✔
INMCM4	✔	✔	✔	✔	✔	✔
IPSL-CM5A-LR	✔	✔	✔	✔	✔	✔
IPSL-CM5A-MR	✔	✔	✔	✔	✔	✔
IPSL-CM5B-LR	✔	✔	✔	✔	✔	✔
MIROC4h			✔		✔	
MIROC5			✔	✔	✔	✔
MIROC-ESM-CHEM	✔	✔	✔	✔	✔	✔
MIROC-ESM	✔	✔	✔	✔	✔	✔
MPI-ESM-LR	✔	✔	✔	✔	✔	✔
MPI-ESM-MR	✔	✔	✔	✔	✔	✔
MPI-ESM-P	✔		✔		✔	
MRI-CGCM3				✔	✔	✔
MRI-ESM1	✔	✔	✔		✔	
NorESM1-ME	✔	✔	✔	✔	✔	✔
NorESM1-M	✔	✔	✔	✔	✔	✔

Of the total ensemble, 15 models were used in the analysis because a full suite of historical and RCP8.5 simulations was available for the net biome production, air temperature and precipitation variables.